



INSTITUT DE FRANCE
Académie des sciences

Comptes Rendus

Géoscience

Sciences de la Planète

Ray Macdonald, Boguslaw Bagiński, Marcin Stachowicz, Harvey E. Belkin, Jan Pawłowski and Jakub Kotowski

Magma mixing and exsolution phenomena in peralkaline rhyolites: insights from the Gold Flat Tuff, Nevada

Volume 353, Special Issue S2 (2021), p. 171-186


Published online: 31 March 2021

Issue date: 28 January 2022

<https://doi.org/10.5802/crgeos.45>

Part of Special Issue: Perspectives on alkaline magmas

Guest editor: Bruno Scaillet (Institut des Sciences de la Terre d'Orléans, CNRS, France)

 This article is licensed under the
CREATIVE COMMONS ATTRIBUTION 4.0 INTERNATIONAL LICENSE.
<http://creativecommons.org/licenses/by/4.0/>



*Les Comptes Rendus. Géoscience — Sciences de la Planète sont membres du
Centre Mersenne pour l'édition scientifique ouverte*

www.centre-mersenne.org

e-ISSN : 1778-7025



Perspectives on alkaline magmas / *Perspectives sur les magmas alcalins*

Magma mixing and exsolution phenomena in peralkaline rhyolites: insights from the Gold Flat Tuff, Nevada

Ray Macdonald^{a, b}, Boguslaw Bagiński^{*, a}, Marcin Stachowicz^a, Harvey E. Belkin^c, Jan Pawłowski^d and Jakub Kotowski^a

^a Department of Geochemistry, Mineralogy and Petrology, University of Warsaw, al. Żwirki i Wigury 93, 02-089 Warszawa, Poland

^b Environment Centre, Lancaster University, Lancaster LA14YQ, UK

^c U.S. Geological Survey retired, 11142 Forest Edge Drive, Reston, VA 20190-4026, USA

^d Biological and Chemical Research Centre, Faculty of Chemistry, University of Warsaw, 02-089 Warszawa, Poland

E-mails: raymacdonald186@gmail.com (R. Macdonald), b.baginski1@uw.edu.pl (B. Bagiński), marcin.stachowicz@uw.edu.pl (M. Stachowicz), harveybelkin@gmail.com (H. E. Belkin), jan.kazimierz.pawlowski@gmail.com (J. Pawłowski), jb.kotowski@gmail.com (J. Kotowski)

Abstract. The distribution and compositions of chevkinite-group minerals (CGMs) in the pantelleritic Gold Flat Tuff, Nevada, USA, are used to examine three aspects of the evolution of the tuff, which we feel are of general significance in peralkaline magmatism. First, both chevkinite-(Ce) and perrierite-(Ce) occur in certain facies, although normally these phases almost invariably occur in different igneous lithologies. Their co-occurrence in the tuff is due to the mixing of pantelleritic and intermediate magmas. Second, the tuff is the first recorded occurrence of a CGM in a pantellerite eruptive, with possible implications for the crystallization conditions. In particular, low values of $a\text{SiO}_2$ may have stabilized ilmenite + chevkinite rather than aenigmatite, although the unusually high LREE contents ($\Sigma\text{La-Sm} \leq 1517$ ppm) in the pantellerite may have played a role. Third, an unusual lamellar texture in the CGM is revealed by Atomic Force Microscopy to be formed by a rutile-like phase. The lamellae may have formed by exsolution from a rutile-like layer in the crystal structure. An electron back-scattered diffraction study of a single crystal showed a structural dislocation not apparent optically or by electron back-scattered imaging. This may have wider implications in mineralogical studies.

Keywords. Gold Flat Tuff, Nevada, Chevkinite-group minerals, Electron back-scattered diffraction, Atomic force microscopy, Magma mixing.

Available online 31st March 2021

* Corresponding author.

1. Introduction

The chevkinite group of REE, Ti-silicates are increasingly being recognized as widespread accessory minerals in a wide range of igneous and metamorphic rocks. Hundreds of localities are known globally, and hundreds more undoubtedly wait to be discovered [Macdonald *et al.*, 2019a]. The two most common members of the group, chevkinite and perrierite, have the general formula $A_4BC_2D_2(Si_2O_7)_2$, where the dominant cations in each site are: A, REE, Ca, Sr; B, Fe^{2+} ; C, Fe^{2+} , Fe^{3+} , Mn, Mg, Ti; D, Ti. In igneous systems, chevkinite and perrierite occupy different paragenesis; chevkinite occurs mainly in evolved, salic rocks, such as syenites and alkali granites (and their extrusive equivalents), and perrierite is known only from rocks of intermediate composition, such as syenodiorites, diorites, latites and trachyandesites [Macdonald and Belkin, 2002, Macdonald *et al.*, 2019a]. Here we report on the unusual case of the occurrence of the two phases in a strongly peralkaline (pantelleritic) rhyolite, which, in addition, is the only record of a chevkinite-group mineral (CGM) crystallizing in a pantelleritic magma.

The CGM under study also displays an unusual textural feature, which has not been reported from the group before. It occurs as lamellae which may be related to some form of exsolution. The lamellae are sufficiently thin ($\leq 2 \mu m$), so that they could not be studied by techniques such as TEM or IR. We chose, therefore, to employ Atomic Force Microscopy (AFM) and electron back-scattered diffraction (EBSD) to examine the nature of the lamellae. The host pantellerite is the Gold Flat Tuff, an ash-flow tuff from the Black Mountain Volcanic Centre in Nevada, USA.

2. Gold Flat Tuff

The multicaldera silicic SW Nevada volcanic field (SWNVF) erupted, over the period 16–7 Ma, more than 20 major ash-flow sheets with the formation of at least eight collapse calderas [Byers Jr *et al.*, 1989, Sawyer *et al.*, 1994]. Associated with the ash-flow tuffs are lava flows and minor pyroclastic rocks which erupted from a large number of smaller vents. The youngest major centre in the field is the Black Mountain Volcanic Centre (BMVC; Figure 1). The centre is

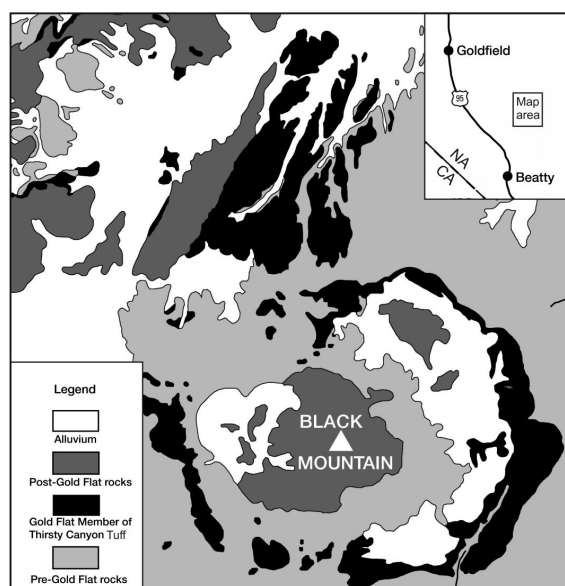


Figure 1. Generalized geological map showing the distribution of the Gold Flat Member of the Thirsty Canyon Group, modified from Noble [1965].

a set of nested collapse structures and constructional volcanoes some 14 km across. Eruptive units of the centre, which are termed the Thirsty Canyon Tuff, comprise ash-flow sheets, lavas and nonwelded tuffs erupted from the Black Mountain caldera between 9.43 and 9.15 Ma [Fleck *et al.*, 1991].

The Gold Flat Tuff is the youngest of the ash-flow sheets (9.15 Ma) in the BMVC, and the only pantelleritic rhyolite in the SW Nevada field, although several earlier BMVC units are comenditic. Noble [1965] reported that the tuff is a compound cooling unit, made up of at least a dozen individual ash-flows in a total thickness of only 30 m and an estimated volume of 20 km^3 [Vogel *et al.*, 1983]. The tuff shows complex vertical and lateral variations in composition and texture, related to a very complex evolutionary history which is still poorly understood. For example, Macdonald *et al.* [2019b] presented mineral chemical evidence, such as a range in feldspar compositions from An_{79-0} and in olivine compositions from $Fo_{54.5-1.9}$, indicating that melts ranging from basaltic through trachyandesitic to comenditic mixed with the pantellerite prior to, or during, eruption.

The pantelleritic component of the tuff has Peralkalinity Indices (P.I.: mol. $(\text{Na}_2\text{O} + \text{K}_2\text{O}/\text{Al}_2\text{O}_3)$) in the range 1.41–1.83 [Macdonald *et al.*, 2019b]. SiO_2 ranges from 70.7 to 73.5 wt% and FeO^* from 5 to 7 wt%. Abundances of MgO and CaO are very low, ≤ 0.03 wt% and ≤ 0.24 wt%, respectively. Notable features are the unusually high contents of F (≤ 2.2 wt%), F + Cl (≤ 2.9 wt%), LREE (La–Sm: ≤ 1517 ppm) and ZrO_2 (≤ 1.04 wt%). We know of no other peralkaline rhyolite with such elevated contents of these elements.

Macdonald *et al.* [2019b] used trachybasalts (belonging to the Basalt of Thirsty Mountain, geographically associated with the Gold Flat Tuff but ~ 4.5 Ma older than it) as proxies for the intermediate component of the tuff. They are $\text{hy} \pm \text{ol} \pm \text{q}$ -normative, with SiO_2 50–51 wt% and Mg-number 0.35–0.46 ($\text{Mg}/(\text{Mg} + \text{Fe})$), with all Fe calculated as Fe^{2+} .

3. Samples and analytical methods

CGMs were studied in two samples of the tuff. Sample GF1 comes from a partially welded tuff, probably of fall origin, at the base of the sheet in Oasis Valley [N37° 05.583' W116° 39.919']. Sample Ttg-hg#1 is from a glassy, welded layer immediately above the basal fall at N37° 20.333' W116° 39.666' and is from the earliest erupted ash flow of the Gold Flat Tuff [Noble, 1965].

Mineral compositions were determined by electron microprobe analysis (EPMA) using a Cameca SX-100 microprobe equipped with four wavelength dispersive spectrometers. The analytical conditions were: accelerating voltage 15 kV and probe current 20–40 nA, with counting times of 20 s on peak and 10 s on each of the two background positions. The standards, crystals and X-ray lines used and generalized detection limits are given in the Appendix. The 'PAP' $\phi(\rho Z)$ program [Pouchou and Pichoir, 1991] was used for corrections. Estimates of analytical precision (1 σ ; wt%) are: Si 0.07, Ti 0.03, Al 0.02, Cr 0.02, Ni 0.03, Fe 0.09, Mn 0.03, Mg 0.04, Ca 0.08, Na 0.01, K 0.01. Representative analyses are given in Table 1; the full data set is given in Supplementary Table 1a.

Analyses were also made of glass in sample GF1 (Supplementary Table 1b). Analyses were conducted with a 10 nA defocused (20 μm) beam. Certain problems can arise with the analysis of glass, related especially to Na volatility. The glass analytical protocol

was optimized by first measuring Na, F and Cl simultaneously, with the interception method to the initial time.

The nature of the lamellar stripes in the CGM was examined using two techniques. Atomic Force Microscopy (AFM) measurements were carried out with a 5500 AFM (Agilent Technologies, Santa Clara, CA, USA). The images were collected in contact mode using PPP-CONT probes (Nanosensors, Neuchâtel, Switzerland) with nominal force constants in the range 0.02–0.77 N/m. Force spectroscopy experiments were performed using AFM PPP-CONT probes. Force versus distance curves were used to obtain the adhesion force with regard to material morphology. Before each experiment, thermal tune methods were employed to determine the spring constants of cantilevers. For each sample, three different 500 nm \times 500 nm squares were probed by force–distance measurements. All experiments were conducted at 23 ± 1 °C.

A diffraction pattern from polished thin sections of chevkinite crystals in sample GF1 exhibiting the lamellar striping feature was captured for Electron Back-Scatter Diffraction (EBSD) analysis. The sample was covered with a 4 nm carbon layer for better surface discharge and measured in a Zeiss Auriga equipped with a Bruker e⁻FlashHR+ detector with integrated ARGUS imaging device. The sample was tilted to 70° using the dedicated stage (tilt about sample *X* axis) for an optimal EBSD signal. Image tilt correction was used on the Zeiss SmartSEM software and no image rotation was applied. The system was calibrated in Bruker ESPRIT 1.9. The crystal was composed of two differently orientated domains, that were measured as Euler angles: $\phi_1 = 169(1)^\circ$, $\Phi = 120(1)^\circ$, $\phi_2 = 141(1)^\circ$ and $\phi_1 = 349(1)^\circ$, $\Phi = 61(3)^\circ$, $\phi_2 = 39(2)^\circ$. The pattern centre (PC), in Bruker fractional coordinates, was measured as $\text{PC}_x = 0.48$, $\text{PC}_y = 0.15$ with a pattern aspect ratio of 1.39 (width/height), detector distance 17.31 mm. Another chevkinite crystal with striping analysed with EBSD had an orientation measured as Euler angles: $\phi_1 = 124.7(9)^\circ$, $\Phi = 42.0(9)^\circ$, $\phi_2 = 197(2)^\circ$; $\text{PC}_x = 0.47$, $\text{PC}_y = 0.47$, detector distance 16.8 mm. The EBSD system uses nonstandard settings of monoclinic unit cells for Euler angle determination. For the chevkinite-type crystal structure it is $a = 11.1 \text{ \AA}$, $b = 13.4 \text{ \AA}$, $c = 5.7 \text{ \AA}$, $\gamma = 79^\circ$. Further analysis and interpretation were conducted with

Table 1. Representative compositions of chevkinite-group minerals

	Chevkinite-(Ce)				Perrierite-(Ce)			
	1	2	3	4	5	6	7	8
wt%								
P ₂ O ₅	bd	0.07	-	-	0.13	0.06	0.05	0.11
Nb ₂ O ₅	1.76	1.13	0.99	1.26	0.15	bd	bd	bd
Ta ₂ O ₅	0.10	0.11	0.11	bd	0.06	0.09	0.13	0.11
SiO ₂	18.70	18.37	19.23	19.85	19.89	20.37	20.62	20.00
TiO ₂	16.70	16.92	17.31	18.87	18.18	19.07	18.92	18.29
ZrO ₂	1.50	0.20	0.37	1.47	0.57	2.03	1.67	0.85
ThO ₂	0.55	0.47	1.15	0.78	2.47	0.71	0.43	0.48
Al ₂ O ₃	bd	bd	0.05	0.27	2.46	2.66	2.69	2.29
Sc ₂ O ₃	bd	bd	-	-	0.24	0.16	0.12	0.19
Y ₂ O ₃	0.48	0.22	0.32	0.38	0.40	0.25	0.22	0.30
La ₂ O ₃	14.41	13.85	12.40	11.94	11.14	11.02	11.53	12.01
Ce ₂ O ₃	21.29	23.32	23.22	21.13	19.25	18.64	19.42	20.57
Pr ₂ O ₃	1.73	1.87	3.00	1.94	1.87	1.35	1.70	1.99
Nd ₂ O ₃	4.38	5.88	6.57	5.47	5.67	4.95	5.08	5.87
Sm ₂ O ₃	0.36	0.41	0.52	0.54	0.77	0.48	0.33	0.52
Gd ₂ O ₃	bd	0.43	0.30	0.32	0.25	bd	0.28	0.44
MgO	0.03	0.04	0.05	0.19	0.88	0.92	0.92	1.14
CaO	3.15	1.52	1.85	4.12	5.01	6.68	6.54	4.85
MnO	0.31	0.27	bd	0.17	0.37	0.24	0.29	0.41
FeO*	10.64	11.38	12.24	11.31	7.80	6.63	6.76	7.32
BaO	bd	bd	-	-	0.14	bd	bd	bd
Total	96.09	96.46	99.68	100.01	97.70	96.31	97.70	97.74
<i>Formulae on the basis of 22 oxygens</i>								
Ca	0.725	0.356	0.418	0.891	1.082	1.415	1.375	1.045
Ba	0.000	0.000	0.000	0.000	0.011	0.000	0.000	0.000
Y	0.055	0.026	0.036	0.041	0.043	0.026	0.023	0.032
La	1.142	1.115	0.964	0.889	0.828	0.804	0.835	0.891
Ce	1.675	1.864	1.792	1.561	1.421	1.349	1.396	1.514
Pr	0.135	0.149	0.230	0.143	0.137	0.097	0.122	0.146
Nd	0.336	0.458	0.494	0.394	0.408	0.350	0.356	0.421
Sm	0.027	0.031	0.038	0.038	0.053	0.033	0.022	0.036
Gd	0.000	0.031	0.021	0.021	0.017	0.000	0.018	0.029
Th	0.027	0.023	0.055	0.036	0.113	0.032	0.019	0.022
Sum A	4.122	4.053	4.048	4.014	4.113	4.106	4.166	4.136

(continued on next page)

Table 1. (continued)

	Chevkinite-(Ce)				Perrierite-(Ce)			
	1	2	3	4	5	6	7	8
Fe ²⁺ (=B)	1.000	1.000	1.000	1.000	1.000	1.000	1.000	1.000
Fe ²⁺	0.912	1.078	1.157	0.909	0.315	0.096	0.110	0.231
Mn	0.056	0.050	0.000	0.029	0.063	0.040	0.048	0.070
Mg	0.010	0.013	0.016	0.057	0.264	0.271	0.269	0.342
Al	0.000	0.000	0.012	0.064	0.584	0.620	0.622	0.543
Sc	0.000	0.000	0.000	0.000	0.042	0.028	0.021	0.033
Zr	0.157	0.021	0.038	0.145	0.056	0.196	0.160	0.083
Nb	0.171	0.112	0.094	0.115	0.014	0.000	0.000	0.000
Ti	0.698	0.778	0.743	0.864	0.755	0.835	0.793	0.765
Sum B	2.004	2.051	2.061	2.183	2.094	2.086	2.022	2.067
Ti (=D)	2.000	2.000	2.000	2.000	2.000	2.000	2.000	2.000
Si	4.018	4.010	4.052	4.006	4.008	4.027	4.047	4.021
P	0.000	0.013	0.000	0.000	0.022	0.010	0.008	0.019
Sum T	4.018	4.023	4.052	4.006	4.031	4.037	4.055	4.040
Σ cations	13.14	13.13	13.16	13.20	13.24	13.23	13.24	13.24

Analyses 3 and 4 from sample Ttg-hg#1, others from GF1. FeO*, all Fe as Fe²⁺; bd, below detection; Dash, not determined. Descriptions of crystals are in Supplementary Table 1.

respect to standard settings of the unit cell axes for chevkinite.

4. Petrography

The pantellerite (Ttg-hg#1) contains 35% modally of megacrysts of feldspar (An₃₉Ab₅₉Or₂–An₀Ab₅₄Or₄₆), quartz, fayalite (Fo_{2–8}), ferrichterite (Mg/(Mg + Fe²⁺) 0.02–0.20), hedenbergite (Ca_{43.6}Mg_{18.6}Fe_{37.9}–Ca_{41.3}Mg_{8.7}Fe_{47.3}), ilmenite (X_{ilm} 94.4–98.1), fluorapatite, CGM and fluorite. With the exception of CGM and fluorite, this is a standard phenocryst assemblage for pantellerites [White *et al.*, 2005, 2009]. The matrix consists of, in addition to the ash matrix, three types of glass (Figure 2a): two (G1 and G2) are pantelleritic and the third (G3) is scarce, poorly phyric or aphyric and comenditic. Sample GF1 contains the same phenocrysts as Ttg-hg#1 except fluorite, and, in addition, phenocrysts of andesine–oligoclase, diopside/augite, forsteritic

olivine, calcic amphibole and zircon. The matrix is almost completely devitrified, such that it is difficult to identify the original glassy components (Figure 2b). However, some phenocrysts have thin glassy rims and there are some small glassy fragments, which we were able to analyse.

White *et al.* [2005] showed that the assemblage of mafic phenocrysts in pantellerites varies with whole-rock peralkalinity; in rocks with P.I. ~1.5–1.8, as in the Gold Flat pantellerite, the phenocryst assemblage is hedenbergite–fayalite–ilmenite–aenigmatite. Amphibole is present when the P.I. is ~1.9. Gold Flat differs, therefore, in that amphibole crystallized at slightly lower P.I. and aenigmatite is absent. The large number of “phenocrysts” in GF1 cannot represent an equilibrium assemblage; Macdonald *et al.* [2019b] argued that the assemblages record magma mixing, the more mafic member in the mixing being of intermediate composition. For example, mixing a magma with SiO₂ content of 60 wt% with a magma of

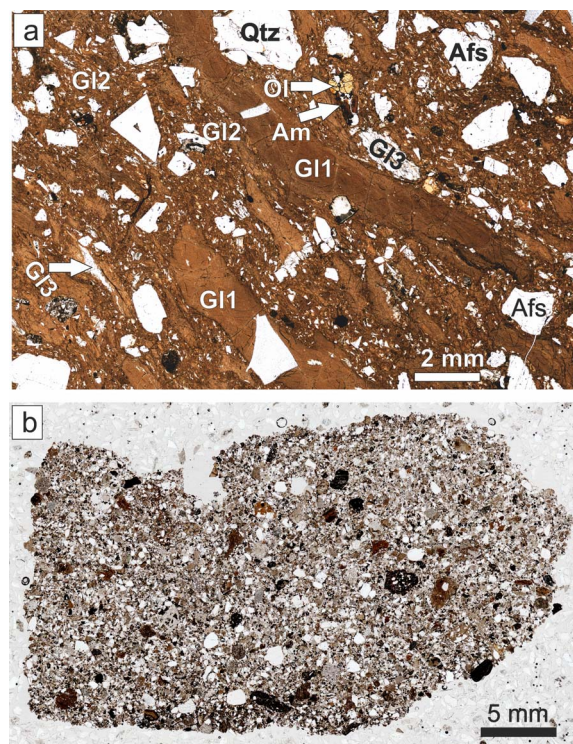


Figure 2. Transmitted-light scans of thin sections of (a) Ttg-hg#1 and (b) GF1. The various types of glass in (a) are described in the text.

Ttg-hg#1 composition (SiO_2 69.6 wt%; Macdonald *et al.*, 2019b) in the proportion 27:73, would produce a magma of GF1 composition (65.5 wt%).

5. Occurrence of CGM

CGMs occur as phenocrysts in both Ttg-hg#1 and GF1, generally forming 10–20 crystals per thin section. They are mainly platy in form, the largest being $114 \times 81 \mu\text{m}$, varying from subhedral to anhedral. They are commonly associated with other phenocrysts (Figures 3a, b). Although some grains are homogeneous on BSE images, the majority show variably complex magmatic zoning (Figure 4). Two types of zoning are most common: oscillatory and sector. The crystal shown in Figure 4a is oscillatory-zoned, with zones showing three main BSE intensities. That shown in Figure 4b also shows magmatic zoning; a compositional profile was made along

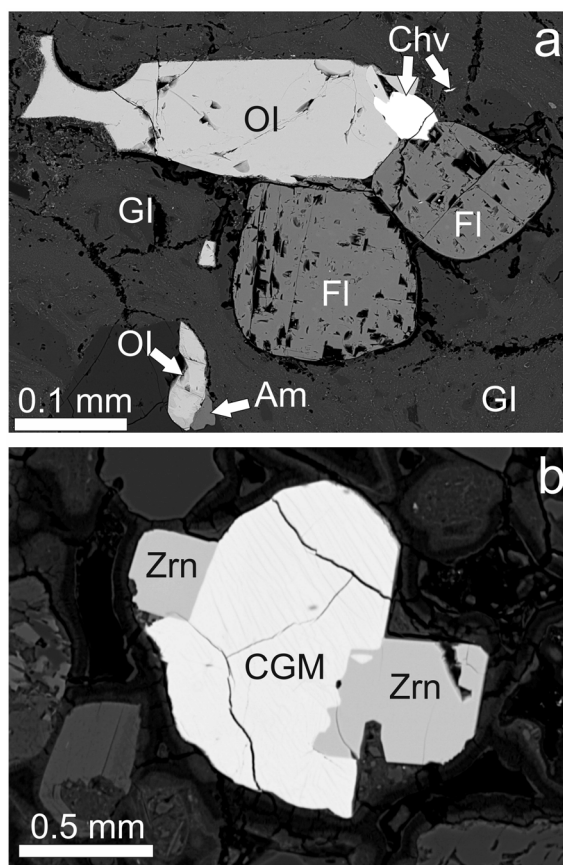


Figure 3. (a) BSE image of chevkinite-(Ce) phenocryst (Chv) associated with olivine and fluorite phenocrysts. Sample Ttg-hg#1. (b) Perrierite-(Ce) associated with phenocrysts of zircon (Zrn). Sample GF1. The CGM shows faint striping, muted by the contrast used.

the marked line (see below). An earlier core with oscillatory zoning has been mantled by a later oscillatory zonation in Figure 4c. A considerably more complex zonation (Figure 4d) shows an unusual “flower-shaped” sector-zoned, dark central zone and a mantling oscillatory-zoned area (upper left).

Most crystals in sample GF1 show, in addition to magmatic zonation, a slight patchiness on BSE images. This is most visible in dark, low-intensity regions, e.g., the upper part of the crystal in Figure 4d and the black patches in the lower-right part of Figure 5d. The patchiness is ascribed below to minor secondary hydration of the crystals (see below).

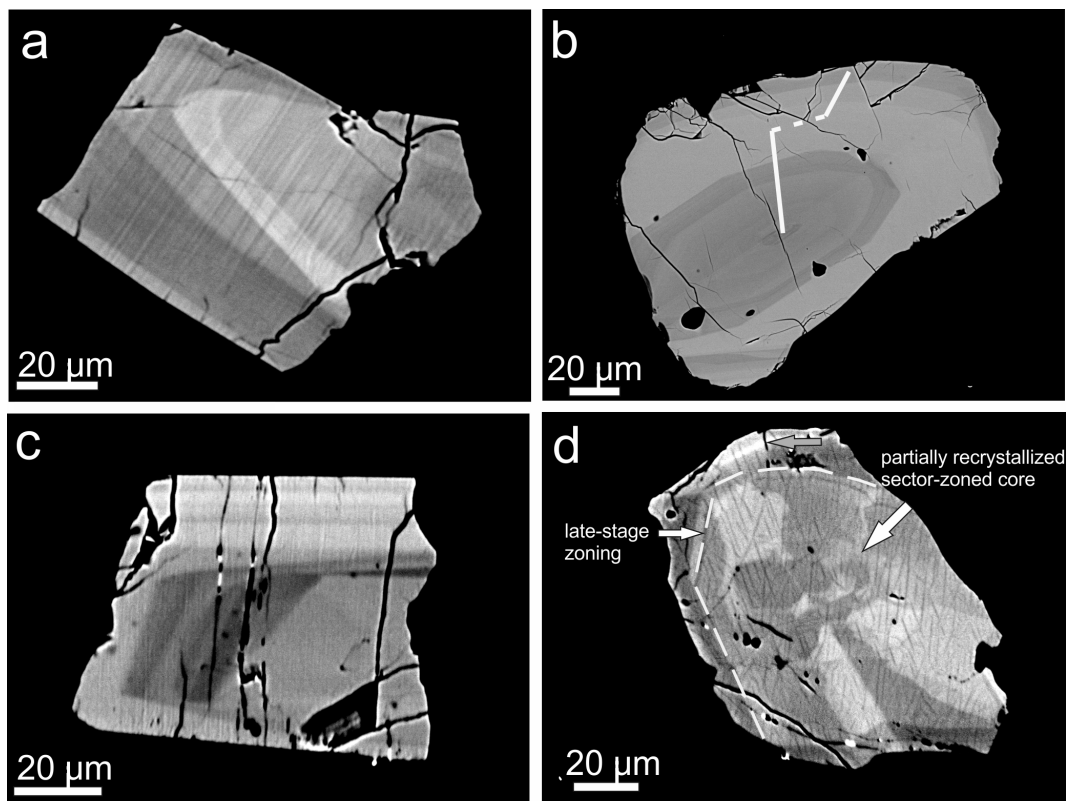


Figure 4. BSE images showing zonation patterns in CGM, all from sample GF1. (a) Oscillatory zonation in chevkinite-(Ce) showing three zones of differing BSE intensity; Supplementary Table 1a, analyses 6–15. (b) Magmatic zonation in chevkinite-(Ce); the compositional range along the marked profile is shown on Figure 6, with the analyses in Supplementary Table 1a, numbers 94–104. (c) Oscillatory zonation formed during two stages of crystallization in chevkinite-(Ce). (d) A partially recrystallized sector-zoned core in perrierite-(Ce) overgrown by an oscillatory-zoned region; analyses 39–50 in Supplementary Table 1a.

An unusual texture is the lamellar striping found in the majority of chevkinite and perrierite crystals, a feature that we have not observed before in CGM. Where present, the feature is restricted to the CGM and is not seen in adjacent crystals (Figures 3a, b). Its apparent absence from some crystals may be a function of the orientation of the texture relative to the thin section cut: the latter may have been parallel to the texture. In Figures 3a and 4b, the contrast used in the BSE images has rather muted the striping, but it is much more clearly visible in Figure 5a. The stripes are 1–2 μm thick, more or less linear, and cut across the compositional zoning. There are variations in the nature of the striping. In Figure 4a, it appears to be perpendicular to the crystal edge. The arrow in

Figure 5a points to a stripe offset. The stripes may (Figure 3a) or may not (Figure 5b) reach the crystal rims. While some stripes are regular and parallel, they may also show dislocations, such as the crystal in Figure 5d.

6. Compositions of CGM

Representative compositions of CGM are presented in Table 1; the full data set is given in Supplementary Table 1a. The minerals are classified using the empirical discriminant of Macdonald *et al.* [2009] (Figure 6). Both chevkinite-(Ce) and perrierite-(Ce) are found in sample GF1, in the approximate ratio 2:1; only chevkinite-(Ce) is present in Ttg-hg#1.

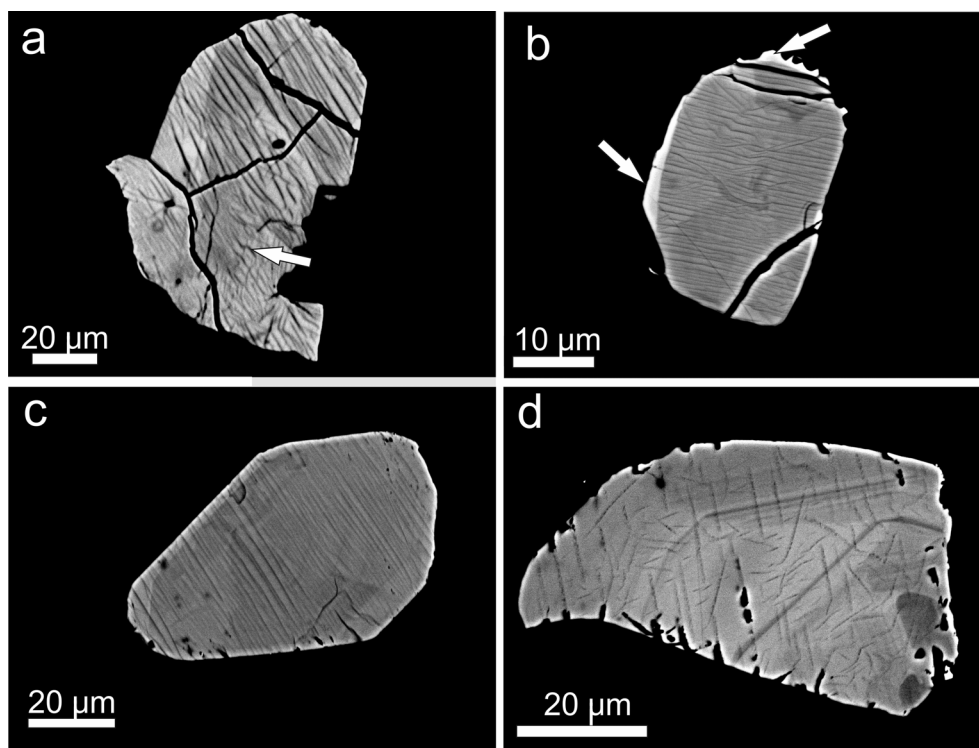


Figure 5. (a) Lamellae strongly developed in partly resorbed chevkinite-(Ce) in sample GF1; Supplementary Table 1a, analyses 65–75. (b) More delicate striping in chevkinite-(Ce), sample Ttg-hg#1. Note that the striping does not reach the bright rim (arrowed). (c) Regular, linear lamellae in perrierite-(Ce), sample GF1. The lamellae reach the rim. (d) Short segments of lamellae cut across oscillatory zoning in chevkinite-(Ce), sample GF1. The darker patches at lower right are slightly more calcic.

Before discussing the compositional features, a comment is required on the analytical totals. In their compilation of 253 analyses of chevkinite and perrierite from the literature, Macdonald *et al.* [2019a] found that the range of analytical totals was 95.5–102.3 wt% (average 98.8 wt%). The low values are due to three effects: (i) some Fe is present in the minerals as Fe^{3+} but is normally reported as Fe^{2+} in EPMA analyses; (ii) the nondetermination of minor elements which can be present at significant levels, e.g., M- and H-REE, Nb, Ta and Hf; and (iii) the incorporation into the structure of H_2O during hydrothermal alteration. In the Gold Flat case, the analytical totals for all determinations range from 93.8 to 101.4 wt% (average 97.3 wt%). The $\text{Fe}^{3+}/\text{Fe}^{2+}$ ratios in the analyses were determined, using stoichiometric criteria, by the method of Droop [1987]; the recalculated FeO and Fe_2O_3 (wt%) and analytical totals are shown in Supplementary Table 1a. The analytical totals now

range from 94.16 to 101.86 wt% (average 97.66 wt%). However, there is an important difference between the minerals in Ttg-hg#1 (chevkinite-(Ce) only) and GF1 (chevkinite-(Ce) and perrierite-(Ce)); the range in Ttg-hg#1 is 99.4–100.5, that in GF1 is 94.2–99.5 wt%. The low values in GF1 are related to the low-BSE-intensity regions in the crystals, as discussed in the Petrography section. This textural feature, and the resulting low totals, are signals of secondary hydration of the minerals [Bagiński *et al.*, 2015]. In Ttg-hg#1, the CGMs are found in nonhydrated pantelleritic glass and have not been secondarily hydrated. GF1 is devitrified and shows signs of late alteration, including an LOI value of 5.41 wt% and the crystals show some signs of the hydration, as noted above.

The chevkinite-(Ce) contains generally higher levels of $\text{La}_2\text{O}_3\text{-Sm}_2\text{O}_3$ (41.02–46.28 wt%) than the perrierite-(Ce) (36.44–40.96 wt%) and also of Nb_2O_5 (0.75–1.76 wt%, b.d. –0.17 wt%, respectively). It also

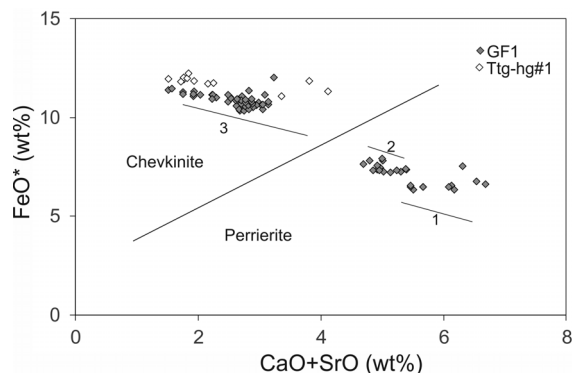


Figure 6. CGM plotted in the empirical discrimination diagram of Macdonald *et al.* [2009]. Data from Supplementary Table 1a. The thin solid lines mark the compositional ranges in three crystals: Supplementary Table 1a, anals 39–50 (=1), 51–61 (=2) and 94–104 (=3; see Figure 4b).

has lower levels of MgO (b.d. -0.40 wt%, 1.35 – 2.11 wt%), Al_2O_3 (b.d. -0.34 wt%, 2.12 – 2.75 wt%) and Sc_2O_3 (b.d. -0.11 wt%, 0.12 – 0.24 wt%). There is a large overlap of ZrO_2 abundances (0.20 – 1.50 wt%, 0.56 – 2.03 wt%). The compositions of both the chevkinite-(Ce) and perrierite-(Ce) are within the ranges compiled from the literature by Macdonald *et al.* [2019a]. In chevkinite-(Ce), $\text{Fe} > \text{Ti}$ in the C site, while $\text{Ti} > \text{Fe}$ in the perrierite-(Ce). Mineral formulae for the least and most calcic analyses can be written:

$(\text{Ce}_{1.86}\text{La}_{1.12}\text{Nd}_{0.46}\text{Ca}_{0.36}\text{Pr}_{0.15})_{3.95}\text{Fe}^{2+}(\text{Fe}^{2+}_{1.08}\text{Ti}_{0.78}\text{Nb}_{0.11})_{1.97}(\text{Si}_2\text{O}_{11})_2$ and $(\text{Ca}_{1.42}\text{Ce}_{1.35}\text{La}_{0.80}\text{Nd}_{0.35}\text{Pr}_{0.10})_{4.02}\text{Fe}^{2+}(\text{Ti}_{0.84}\text{Al}_{0.62}\text{Zr}_{0.20}\text{Mg}_{0.27}\text{Fe}^{2+}_{0.10})_{2.03}(\text{Si}_2\text{O}_{11})_2$ (Table 1, anals 2 and 6, respectively). Individual crystals show significant parts of the compositional range (Figure 6), including the profile shown in Figure 4b.

7. Nature and formation of lamellae

The fine scale of the lamellar stripes (1 – 2 μm) means that their microprobe analyses are invariably composites of lamella and adjacent crystal. An attempt, therefore, was made to determine their nature using element maps (Figure 7). On the maps, the lamellae are higher in Ti, and to a lesser extent Fe (not shown), and lower in Si, than the host CGM. Those features suggested the possible presence of a TiO_2 phase. An

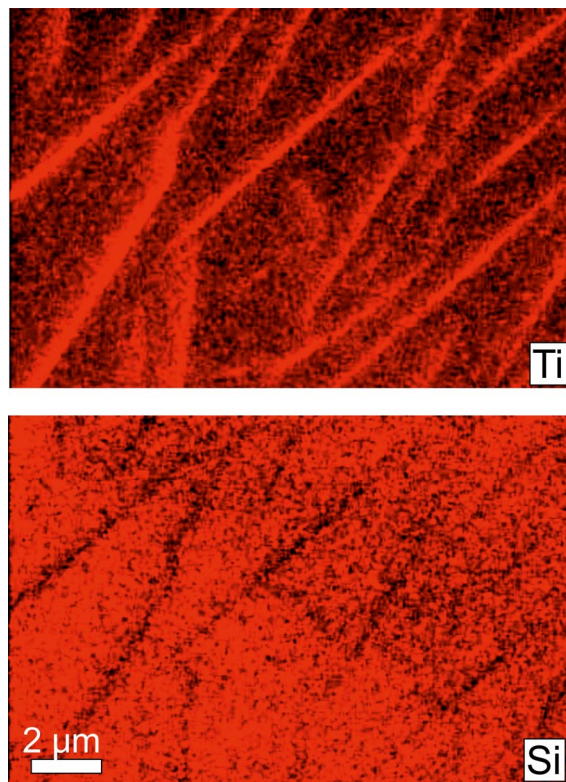


Figure 7. False-colour element maps (Ti and Si) of striping in part of crystal shown in Figure 4a.

attempt was made, therefore, to characterize the Ti-rich zones using Atomic Force Microscopy (AFM).

AFM images of reference rutile and chevkinite-(Ce) free of stripes present similar, even surface topography. In contrast, an image of GF1 chevkinite-(Ce) revealed a stripe-like organization with two distinct domains; the surface topography is displayed as a pseudocolour plot in Figure 8, where the chevkinite domain with grain-like features is separated by lamellar Ti-rich structures. We cautiously suggest that the lamellar structures have an increased degree of disorder and are not fully crystalline. The histograms of counts against adhesion force were determined for a reference chevkinite and showed that its adhesion force range is 3 – 4 nN, and for a reference rutile to be 4 – 8 nN. The range across the lamellae is 3 – 6 and is taken to be a superposition of chevkinite and rutile histograms. The Ti-rich lamellae would appear, therefore, to consist at least partly of a rutile-like phase.

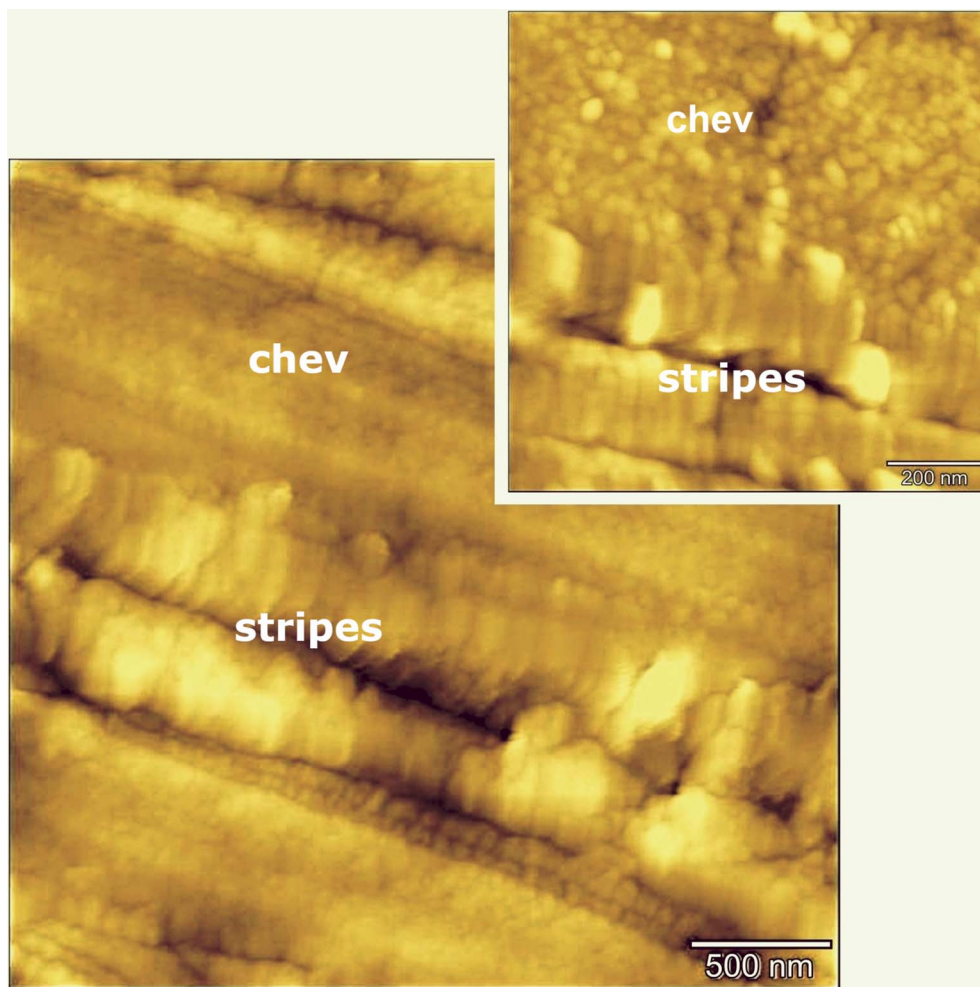


Figure 8. Surface topography of lamellae in chevkinite-(Ce) determined by AFM. Domains related to the host mineral and the stripes are shown. The crystal is that shown in Figure 5b.

The fact that the lamellae are oriented argues for subsolidus precipitation, perhaps by exsolution. Rutile has been recorded as exsolution inclusions in several phases, including biotite [Shau *et al.*, 1991], garnet [Hwang *et al.*, 2007, Keller and Ague, 2019], titanian columbite [Černý *et al.*, 2007], quartz [Adachi *et al.*, 2010] and gem corundum [Palke and Breeding, 2017]. It most commonly occurs as oriented needles, indicating a crystallographic control on the exsolution [Keller and Ague, 2019]. Several workers have drawn attention to the presence of a rutile-like layer in CGM, e.g., Calvo and Faggiani [1974], Gueho *et al.* [1995], Li *et al.* [2005] and Holtstam *et al.* [2017]. In Figure 9, the top panel shows the crystal structure of

rutile and the bottom panel shows chevkinite with a rutile-like layer in the centre. The layer is formed by CO_6 and DO_6 distorted coordination octahedra, the distortion making the oxygen atoms (red) misaligned compared to the rutile arrangement. We speculate that the rutile lamellae in the Gold Flat CGM formed along this rutile-like layer, which might have been energetically/kinetically favourable sites for rutile nucleation.

There are, however, some problems with this proposal. Concentration of Ti in the lamellae should have left neighbouring areas depleted in Ti, but this is not obvious on the chemical maps (Figure 7). A cautious conclusion, therefore, is that during cooling of

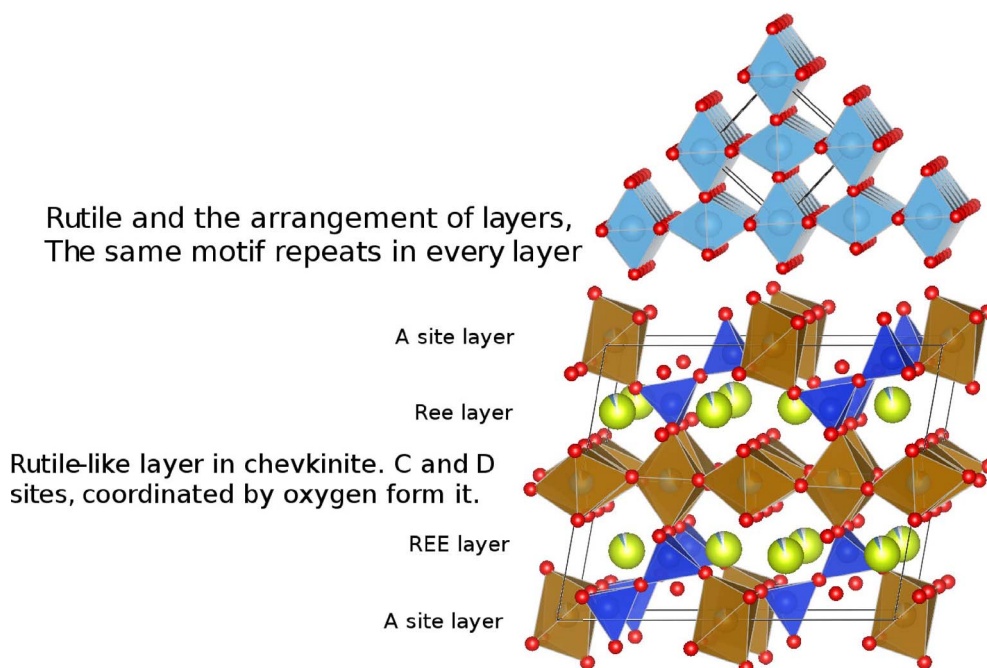


Figure 9. Arrangement of layers in rutile (upper) and a visualization of the rutile-like layer in chevkinite.

the magmas, the CGM structure in both chevkinite-(Ce) and perrierite-(Ce) became unstable and exsolved a rutile-like phase along the rutile-like layer. That does not, however, explain why the lamellar striping is, in our experience, restricted to the Gold Flat Tuff; neither is it clear what promoted the exsolution.

An EBSD study revealed an unexpected aspect of the chevkinite-(Ce) structure. The crystal shown in Figure 10a shows a distinct, if minor, change in direction of the stripes along a line orientated NW–SE. The crystal consists of two structural domains, with one domain rotated relative to the other, as shown by the orientation of the *a*, *b* and *c* axes. The stripes are perpendicular to the crystallographic unit cell direction $b = 5.7 \text{ \AA}$. The grey MO_6 octahedra are parallel to the *ab* crystallographic plane from rutile-like layers in the chevkinite-(Ce) structure. In contrast, the crystal in Figure 10b showing regular, linear stripes does not have the two-domain structure. It is unknown what caused the rotation of the structure in Figure 10a, but it is important to note that its existence was not visible in standard optical and BSE imaging, being revealed only by EBSD. The result raises the possibil-

ity that such structural dislocations occur more frequently than presently understood.

8. Discussion

8.1. Paragenesis of the CGM

Using a $(\text{CaO} + \text{SrO} + \text{MgO} + \text{Al}_2\text{O}_3) - \Sigma(\text{La}_2\text{O}_3 - \text{Sm}_2\text{O}_3) - \text{FeO}^*$ plot, Macdonald and Belkin [2002] showed that in igneous rocks chevkinite generally occurs in evolved rock types, such as rhyolites, granites and nepheline syenites, whereas perrierite is normally found in intermediate rocks. In such a plot (Figure 11), the Gold Flat CGM form two clusters, consistent with formation in different magmas, as already shown by the different phenocryst assemblages. Also shown are perrierites from rocks of intermediate (broadly trachyandesitic) composition, suggesting that more perrieritic minerals at Gold Flat are also formed from intermediate magmas. This is confirmed by the analyses of glassy fragments and crystal rims in GF1 (Supplementary Table 1b). Important features of the analyses are: (i) Some of the analytical totals are low (92.2–100.5 wt%), which can be ascribed to secondary hydration of the glass; (ii) There

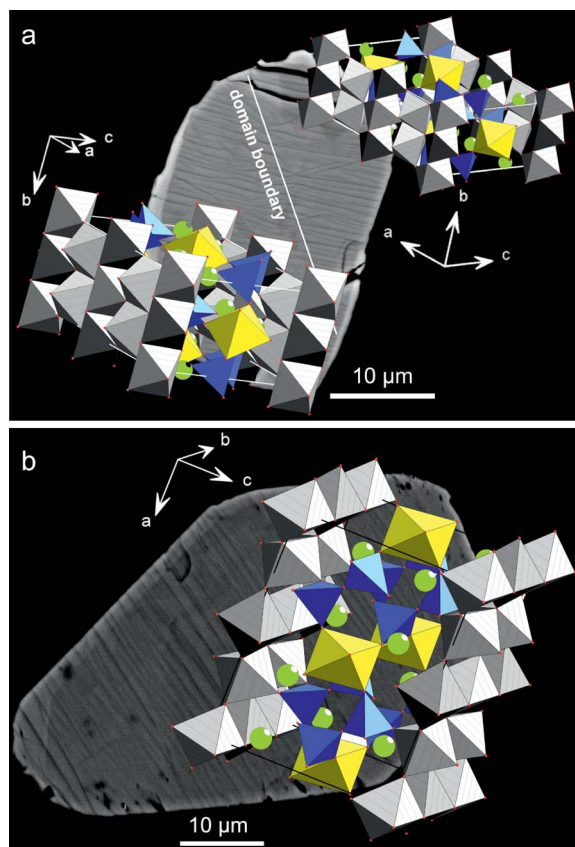


Figure 10. (a) Rotation of the structure in a chevkinite-(Ce) crystal revealed by EBSD, the boundary between the two domains coinciding with minor displacements of the lamellae. The crystal is that shown in Figure 5b. (b) In the crystal (Figure 5c), the lamellae are regular and the structure is not rotated.

has clearly been some mobilization of the alkalis and Ca; (iii) Aluminium, Ti (Figure 12) and Fe show negative trends, and Na a positive trend, plotted against SiO_2 ; (iv) The spread of data encloses for all elements the composition of a trachytic melt inclusion found in a clinopyroxene in a feldspar cluster [Macdonald *et al.*, 2019b]. In the SiO_2 -alkalis classification, the analyses (with SiO_2 in the range 64.8–66.8 wt%, calculated anhydrous to 100%) plot in the trachyte field, close to the border with trachyandesite.

With the caveat that the vertical and lateral variations in lithology in the Gold Flat tuff are not well constrained, the following crystallization history of

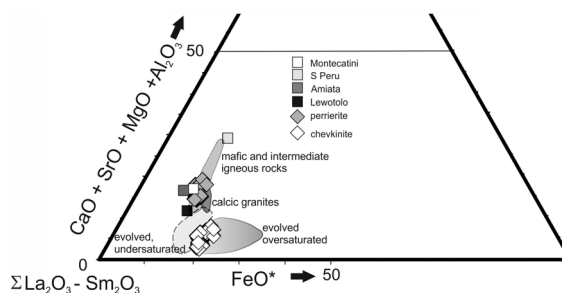


Figure 11. Triangular plot to show the different paragenesis of chevkinite and perrierite (slightly simplified from Macdonald and Belkin, 2002). Data from Supplementary Table 1a. Perrierites from various “trachyandesitic” hosts overlap the Gold Flat field: Mt Amiata, Italy [Van Bergen, 1984]; Montecatini, Italy [Cellai *et al.*, 1993]; Lewotolo, Indonesia [De Hoog and van Bergen, 2000]; southern Peru [Carlier and Lorand, 2008].

CGM in the tuff can be proposed. As shown by glass analyses in sample Ttg-hg#1, the tuff comprises pantelleritic and comenditic magmas. Using various SiO_2 plots, Macdonald *et al.* [2019b] showed that the two magmas had evolved along different trends and were derived from two evolving magma reservoirs. As discussed above, there is also petrographic, and mineral and glass compositional, evidence that intermediate magmas were components in the tuff.

Some information on the crystallization history comes from crystal zoning. Most common in the CGM is oscillatory zoning (Figures 4a, b), generally ascribed to repetitive kinetic effects during crystallization [Paterson and Stephens, 1992, Tepper and Kuehner, 1999]. The other type, particularly well shown in Figure 4d, is sector zoning and we suggest that the texture in that image represents a sector-zoned core which was partially recrystallized during a later stage of crystallization. Sector zoning has been ascribed to slow growth and low diffusivity during crystallization [Schaltegger *et al.*, 1999, Watson and Liang, 1995]. A possible model for the Gold Flat case is, therefore, of a relatively prolonged stage of perrierite-(Ce) growth in an intermediate magma and chevkinite-(Ce) in a pantelleritic magma, followed by more rapid changes promoting oscillatory zoning around the core and recrystallization of the core before magma mixing. The intermediate magma

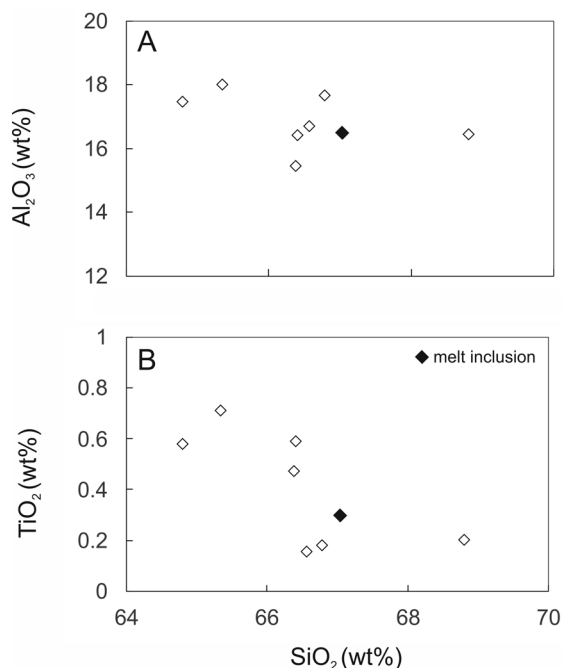


Figure 12. SiO₂ plotted against (a) Al₂O₃ and (b) TiO₂ in matrix glass from GF1. Data from Supplementary Table 1b, recalculated to 100% anhydrous. Also shown is the composition of a trachytic melt inclusion from the Gold Flat Tuff [Macdonald *et al.*, 2019b].

was then mingled with the chevkinite-(Ce)-bearing pantellerite magma but with insufficient time before eruption for new mantles to form on existing crystals.

8.2. Formation of chevkinite-(Ce) in a pantellerite

It was noted earlier that the Gold Flat Tuff is the only pantelleritic extrusive known to carry CGM phenocrysts. Possible explanations for this unusual paragenesis are that it was related to a compositional effect or unusual P–T–*f*O₂–*a*SiO₂ conditions of crystallization. For example, the high LREE contents (La–Sm ≤1517 ppm; Macdonald *et al.*, 2019b), the highest levels in a pantellerite of which we are aware, may have been a critical factor in forming the chevkinite-(Ce). However, chevkinite is a common phase in the comendites in the BMVC which have lower LREE contents (≤600 ppm) than the pantellerite (e.g., Vogel *et al.*, 1983, 1989). Unfortunately, no compositional

or structural information is available on these phases and it is possible that they are antecrystic perrierite, able to crystallize from magmas poorer in REE.

Alternatively, the appearance of CGM may have been related to the crystallization conditions. Little is known about the P–T conditions under which the various Gold Flat magmas evolved, but Macdonald *et al.* [2019b] cautiously suggested, on the basis of comparisons with high P–T experiments on compositionally similar pantellerites from Eburru, Kenya [Scaillet and Macdonald, 2006] and Pantelleria [Di Carlo *et al.*, 2010], that the pantelleritic magma started crystallizing at a temperature of ~740 °C, close to or at water saturation, at *f*O₂ below FMQ. However, the Kenyan and Pantescan rocks and the experiments did not form chevkinite under any conditions. In contrast, Scaillet and Macdonald [2001] synthesized chevkinite-(Ce) in two comendites from the Olkaria complex, Kenya, although its stability field was poorly constrained.

However, the explanation for the formation of chevkinite-(Ce) may lie in the absence of aenigmatite from the Gold Flat pantellerite. On the basis of thermodynamic modelling, Macdonald *et al.* [2011] found the antipathetic relationship between fayalite and aenigmatite to be a function of *T*, *P* and *a*SiO₂, with aenigmatite crystallizing at the expense of fayalite at *T* < 750 °C at *a*SiO₂ close to quartz saturation at 150 MPa. Macdonald *et al.* [2011] showed that the aenigmatite–phyric pantellerites of Pantelleria crystallized at *a*SiO₂ = 1. Using the QUILF programme from olivine–magnetite–ilmenite equilibrium, Andersen *et al.* [1993], Macdonald *et al.* [2019b] calculated the *a*SiO₂ relative to quartz saturation for the Gold Flat pantellerite to be 0.633 at *P* = 1000 bar, potentially favouring the absence of aenigmatite in favour of fayalite + ilmenite. Titanium was not, therefore, partitioned into aenigmatite but instead partitioned between ilmenite and chevkinite-(Ce). In addition to its unusual compositional features and complex evolutionary history, the Gold Flat Tuff pantellerite may have crystallized in an unusual corner of P–T–*f*O₂–*a*SiO₂ space.

9. Conclusions

The study has revealed unusual features of the occurrence and textures of CGM which may be of more general significance in studies of accessory minerals.

More generally, we suggest that the use of AFM will offer to geologists another technique to apply to the study of such phases.

- (1) The coexistence of chevkinite-(Ce) and perrierite-(Ce) in the Gold Flat Tuff was a result of the mixing of pantelleritic and intermediate magmas.
- (2) The unique occurrence of a CGM in a pantelleritic extrusive may have been due to the host magmas crystallizing at a relatively low $a\text{SiO}_2$, favouring the formation of ilmenite and chevkinite rather than aenigmatite. The unusually high contents of LREE may also have played a role in its formation.
- (3) An unusual lamellar texture in the CGM, not previously recorded in the group, may have formed by exsolution of a Ti-rich phase from a rutile-like layer in the crystal structure. We provide no explanation of why the texture has been described only from the Gold Flat Tuff.
- (4) An EBSD study unexpectedly revealed a structural rotation in the crystal, which was not visible optically or by electron back-scattered imaging. The phenomenon may be of wider occurrence than currently recognized.
- (5) Zonation patterns in the CGM have established a complex pre-eruptive evolutionary history in the magma reservoir.

Acknowledgements

We thank Bruno Scaillet for the invitation to contribute this paper to the Special Issue and Donald C. Noble for supplying the sample of Ttg-hg#1. We also thank Lidia Ježak and Petras Jokubauskas (EPMA) and Marcin Syczewski (SEM) for analytical support. Two anonymous reviewers provided very helpful comments and suggestions, which are much appreciated. The research was funded by National Science Centre, Poland, grant number 2017/26/M/ST10/00407. The work was also supported through the Innovative Economy Operational Program POIG.02.02.00-00-409 025/09 (NanoFun; Cryo-SEM microscopy lab).

Supplementary data

Supporting information for this article is available on the journal's website under <https://doi.org/10.5802/crgeos.45> or from the author.

Appendix

Table 2. Analytical conditions for chevkinite-(Ce)

Element	Line	Crystal	Standard	Approx. detection limit (wt%)
Al	K α	TAP	Orthoclase	0.01
Ba	L α	LiF	Barite	0.12
Ca	L α	PET	CaSiO ₃	0.01
Ce	K α	PET	CeP ₅ O ₁₄	0.04
Fe	K α	LiF	Haematite	0.04
Gd	L β	LiF	GdP ₅ O ₁₄	0.19
La	L α	PET	LaB ₆	0.04
Mg	K α	TAP	Diopside	0.01
Mn	K α	LiF	Rhodonite	0.04
Nb	L α	PET	Nb metal	0.05
Nd	L β	LiF	NdP ₅ O ₁₄	0.18
P	K α	PET	Apatite Jap2	0.02
Pr	L β	LiF	PrP ₅ O ₁₄	0.12
Sc	K α	PET	Sc metal	0.01
Si	K α	TAP	Wollastonite	0.01
Sm	L β	LiF	SmP ₅ O ₁₄	0.19
Ta	M α	TAP	Ta metal	0.04
Th	M α	PET	ThO ₂ Synthetic	0.09
Ti	K α	PET	Rutile	0.02
Y	L α	TAP	Y ₃ Al ₅ O ₁₂	0.04
Zr	L α	PET	Zircon ED2	0.05

Data for accel. voltage 15 kV, probe current 50 nA.

References

- Adachi, T., Hokada, T., Osanai, Y., Toyoshima, T., Baba, S., and Nakano, N. (2010). Titanium behaviour in quartz during retrograde hydration: Occurrence of rutile exsolution and implications for

- metamorphic processes in the Sør Rondane Mountains, East Antarctica. *Polar Sci.*, 3, 222–234.
- Andersen, D. J., Lindsley, D. H., and Davidson, P. M. (1993). A Pascal program to assess equilibria among Fe-Mg-Mn-Ti oxides, pyroxene, olivine, and quartz. *Comp. Geosci.*, 19, 1333–1350.
- Bagiński, B., Macdonald, R., Dzierżanowski, P., Zozulya, D., and Kartashov, P. M. (2015). Hydrothermal alteration of chevkinite-group minerals: products and mechanisms. Part 1. Hydration of chevkinite-(Ce). *Mineral. Mag.*, 79, 1019–1037.
- Byers Jr, F. M., Carr, W. J., and Orkild, P. P. (1989). Volcanic centers of southwestern Nevada: Evolution of understanding, 1960–1988. *J. Geophys. Res.*, 94, 5908–5924.
- Calvo, C. and Faggiani, R. (1974). A re-investigation of the crystal structures of chevkinite and perrierite. *Am. Mineral.*, 59, 1277–1285.
- Carrier, G. and Lorand, J.-P. (2008). Zr-rich accessory minerals (titanite, perrierite, zirconolite, baddeleyite) record strong oxidation associated with magma mixing in the south Peruvian potassic province. *Lithos*, 104, 54–70.
- Cellai, D., Conticelli, S., and Diella, V. (1993). Perrierite-chevkinite in igneous ultrapotassic rocks from Central Italy: chemical data and their petrological significance. *Per. Mineral.*, 62, 57–66.
- Černý, P., Novák, M., Chapman, R., and Ferreira, K. J. (2007). Subsolidus behavior of niobian rutile from the Písek region, Czech Republic: a model for exsolution in W- and Fe²⁺ >> Fe³⁺-rich phases. *J. Geosci.*, 52, 143–159.
- De Hoog, J. C. M. and van Bergen, M. J. (2000). Volatile-induced transport of HFSE, REE, Th and U in arc magmas: evidence from zirconolite-bearing vesicles in potassic lavas of Lewotolo volcano (Indonesia). *Contrib. Mineral. Petrol.*, 139, 485–502.
- Di Carlo, I., Rotolo, S. G., Scaillet, B., Buccheri, V., and Pichavant, M. (2010). Phase equilibrium constraints on pre-eruptive conditions of recent felsic explosive volcanism at Pantelleria Island, Italy. *J. Petrol.*, 51, 2245–2276.
- Droop, G. T. R. (1987). A general equation for estimating Fe³⁺ concentrations in ferromagnesian silicates and oxides from microprobe analyses, using stoichiometric criteria. *Mineral. Mag.*, 51, 431–435.
- Fleck, R. J., Lanphere, M. A., Turrin, B., and Sawyer, D. A. (1991). Chronology of late Miocene to Quaternary volcanism and tectonism in the southwest Nevada volcanic field (abs.). *Geol. Soc. Am. Abstracts with Programs*, 23(2), 25.
- Gueho, C., Giaquinta, D., Mansot, J. L., Ebel, T., and Palvadeau, P. (1995). Structure and magnetism of La₄Mn₅Si₄O₂₂ and La₄V₅Si₄O₂₂: two new rare-earth transition metal sorosilicates. *Chem. Mater.*, 7, 486–492.
- Holtstam, D., Bindi, L., Hålenius, U., and Andersson, U. B. (2017). Delhuyarite-(Ce) – Ce₄Mg(Fe³⁺₂W)□(Si₂O₇)₂O₆(OH)₂ – a new mineral of the chevkinite group, from the Nya Bastnäs Fe-Cu-REE deposit, Sweden. *Eur. J. Mineral.*, 29, 897–905.
- Hwang, S. L., Yui, T. F., Chu, H. T., Shen, P., Schertl, H. P., Zhang, R. Y., and Liou, J. G. (2007). On the origin of oriented rutile needles in garnet from UHP eclogites. *J. Met. Geol.*, 25, 349–362.
- Keller, D. S. and Ague, J. J. (2019). Crystallographic and textural evidence for precipitation of rutile, ilmenite, corundum, and apatite lamellae from garnet. *Am. Mineral.*, 104, 980–995.
- Li, G., Yang, G., Ma, Z., Shi, N., Xiong, M., Fan, H., and Sheng, G. (2005). Crystal structure of natural non-metamict Ti- and Fe²⁺-rich chevkinite-(Ce). *Acta Geol. Sinica*, 79, 325–331.
- Macdonald, R., Bagiński, B., Belkin, H. E., and Stachowicz, M. (2019a). Composition, paragenesis and alteration of the chevkinite group of minerals. *Am. Mineral.*, 104, 349–367.
- Macdonald, R., Bagiński, B., Belkin, H. E., White, J. C., and Noble, D. C. (2019b). The Gold Flat Tuff, Nevada: insights into the evolution of peralkaline silicic magmas. *Lithos*, 328–329, 1–13.
- Macdonald, R., Bagiński, B., Leat, P. T., White, J. C., and Dzierżanowski, P. (2011). Mineral stability in peralkaline silicic rocks: Information from trachytes of the Menengai volcano, Kenya. *Lithos*, 125, 553–568.
- Macdonald, R. and Belkin, H. E. (2002). Compositional variation in minerals of the chevkinite group. *Mineral. Mag.*, 66, 1075–1098.
- Macdonald, R., Belkin, H. E., Wall, F., and Bagiński, B. (2009). Compositional variation in the chevkinite group: new data from igneous and metamorphic rocks. *Mineral. Mag.*, 73, 777–796.
- Noble, D. C. (1965). Gold Flat Member of the Thirsty Canyon Tuff – a pantellerite ash-flow sheet in

- southern Nevada. *US Geol. Surv. Prof. Paper*, 525-B, B85–B90.
- Palke, A. C. and Breeding, C. M. (2017). The origin of needle-like rutile inclusions in natural gem corundum: A combined EPMA, LA-ICP-MS, and nanoSIMS investigation. *Am. Mineral.*, 102, 1451–1461.
- Paterson, B. A. and Stephens, W. E. (1992). Kinematically-induced compositional zoning in titanite: Implications for accessory-phase/melt partitioning of trace elements. *Contrib. Mineral. Petrol.*, 109, 373–395.
- Pouchou, J. L. and Pichoir, J. F. (1991). Quantitative analysis of homogeneous or stratified microvolumes applying the model 'PAP'. In Heinrich, K. F. J. and Newbury, D. E., editors, *Electron Probe Quantification*, pages 31–75. Plenum Press, New York.
- Sawyer, D. A., Fleck, R. J., Lanphere, M. A., Warren, R. G., Broxton, D. E., and Hudson, M. R. (1994). Episodic caldera volcanism in the Miocene southwestern Nevada volcanic field: Revised stratigraphic framework, $^{40}\text{Ar}/^{39}\text{Ar}$ geochronology, and implications for magmatism and extension. *Geol. Soc. Am. Bull.*, 106, 1304–1318.
- Scaillet, B. and Macdonald, R. (2001). Phase relations of peralkaline silicic magmas and petrogenetic implications. *J. Petrol.*, 42, 825–845.
- Scaillet, B. and Macdonald, R. (2006). Experimental constraints on pre-eruption conditions of pantelleritic magmas: evidence from the Eburru complex, Kenya Rift. *Lithos*, 91, 95–108.
- Schaltegger, U., Fanning, C. M., Günther, D., Maurin, J. C., Schulmann, K., and Gebauer, D. (1999). Growth, annealing and recrystallization of zircon and preservation of monazite in high-grade metamorphism: conventional and in-situ U-Pb isotope, cathodoluminescence and microchemical evidence. *Contrib. Mineral. Petrol.*, 134, 186–201.
- Shau, Y. H., Yang, H. Y., and Peacor, D. R. (1991). On oriented titanite and rutile inclusions in sagenitic biotite. *Am. Mineral.*, 76, 1205–1217.
- Tepper, J. H. and Kuehner, S. C. (1999). Complex zonation in apatite from the Idaho batholith: A record of magma mixing and intra-crystalline trace element diffusion. *Am. Mineral.*, 84, 581–595.
- Van Bergen, M. J. (1984). Perrierite in siliceous lavas from Mt Amiata, central Italy. *Mineral. Mag.*, 48, 553–556.
- Vogel, T. A., Noble, D. C., and Younker, L. W. (1983). *Chemical evolution of a high-level magma system: the Black Mountain volcanic center, southern Nevada*. Report No. UCRL-53444. Lawrence Livermore National Laboratory, Livermore, California.
- Vogel, T. A., Noble, D. C., and Younker, L. W. (1989). Evolution of a chemically zoned magma body: Black Mountain volcanic center, southwestern Nevada. *J. Geophys. Res.*, 94, 6041–6058.
- Watson, E. B. and Liang, Y. (1995). A simple model for sector zoning in slowly grown crystals: implications for growth rate and lattice diffusion, with emphasis on secondary minerals in crustal rocks. *Am. Mineral.*, 80, 1179–1187.
- White, J. C., Parker, D. F., and Ren, M. (2009). The origin of trachyte and pantellerite from Pantelleria, Italy: Insights from major element, trace element, and thermodynamic modelling. *J. Volcanol. Geotherm. Res.*, 179, 33–55.
- White, J. C., Ren, M., and Parker, D. F. (2005). Variation in mineralogy, temperature, and oxygen fugacity in a suite of strongly peralkaline lavas and tuffs, Pantelleria, Italy. *Can. Mineral.*, 43, 1331–1347.